MATERIALS SCIENCE

Nitrogen cluster doping for high-mobility/conductivity graphene films with millimeter-sized domains

Li Lin[1]*, Jiayu Li[2,3,4]*, Qinghong Yuan[5,6]*, Qiucheng Li[1,4]*, Jincan Zhang[1,4], Luzhao Sun[1,4], Dingran Rui[2], Zhaolong Chen[1], Kaicheng Jia[1], Mingzhan Wang[1], Yanfeng Zhang[1,7], Mark H. Rummeli[8,9,10], Ning Kang[2], H. Q. Xu[2†], Feng Ding[11,12†], Hailin Peng[1,13†], Zhongfan Liu[1,13†]

Directly incorporating heteroatoms into the hexagonal lattice of graphene during growth has been widely used to tune its electrical properties with superior doping stability, uniformity, and scalability. However the introduction of scattering centers limits this technique because of reduced carrier mobilities and conductivities of the resulting material. Here, we demonstrate a rapid growth of graphitic nitrogen cluster–doped monolayer graphene single crystals on Cu foil with remarkable carrier mobility of 13,000 cm^2 V^{-1} s^{-1} and a greatly reduced sheet resistance of only 130 ohms square^{-1}. The exceedingly large carrier mobility with high n-doping level was realized by (i) incorporation of nitrogen-terminated carbon clusters to suppress the carrier scattering and (ii) elimination of all defective pyridinic nitrogen centers by oxygen etching. Our study opens up an avenue for the growth of high-mobility/conductivity doped graphene with tunable work functions for scalable graphene-based electronic and device applications.

INTRODUCTION

Although the rich electrical and optical properties of graphene make it promising for utilization in various applications as a key material, one of the primary industrial requirements is a cost-efficient and scalable technique to gain precise control over the doping levels without reducing the carrier mobility and stability of graphene (1–3), which has not yet been established (3, 4). The existing routes to achieve controllability of graphene doping levels mainly entail external gates and adsorbed chemical dopants (5–7), both of which share the drawbacks of lacking environmental stability and industrial scalability. By directly introducing foreign atoms into the graphene lattice, the chemical vapor deposition (CVD) approach can facilitate the large-scale production of graphene films with high doping uniformity and stability (2, 8–10). However, such an approach is currently severely limited by the greatly reduced carrier mobilities caused by the introduction of a large number of charge scattering centers (11). Therefore, the conductivity of doped graphene is much lower than what it was expected (2, 8), severely hindering the commercial applications of graphene, such as the transparent conductive film (3, 12, 13).

Charge scattering by dopants is sensitive to the bonding configuration of the heteroatoms (e.g., graphitic N, pyridinic N, and pyrrolic N in nitrogen-doped graphene). Among all the possible nitrogen-doping configurations, the graphitic N doping could result in n-doping effect and preserve the high carrier mobility due to minor distortion of the graphene lattice (11, 14). Unfortunately, precise control over the atomic configuration and spatial arrangement of N-dopants in graphene is still a big challenge. Besides bond configuration, the spatial arrangement of the dopants also affects the scattering greatly. It has been theoretically predicted that the clusterization of the charged impurities in graphene would notably suppress their contribution to resistivity (15), which is also applicable in other two-dimensional (2D) materials (16). Another important but less notable feature responsible for the low carrier mobility is the presence of a high density of grain boundaries that scatter the carriers in the doped polycrystalline graphene films (17). All these, in turn, present a higher demand of synthetic controllability in graphene-doping methodologies.

Here, in sharp contrast to the common nitrogen-doped graphene samples in which mixed pyridinic nitrogen and graphitic nitrogen coexist (Fig. 1A) (2), we successfully synthesized in-plane graphitic nitrogen cluster–doped graphene (Nc-G) with millimeter-sized single crystalline domains, relying on an oxygen-assisted CVD growth strategy to eliminate the pyridinic N and to suppress the nucleation density and using acetonitrile (ACN) as both nitrogen and carbon sources (fig. S1). It was found that each doping center in the Nc-G contains three to six or even more graphitic nitrogen dopants in a triangular in-plane shape (Fig. 1B). Because of the unique spatial arrangement of dopants, a remarkable high carrier mobility of 13,000 cm^2 V^{-1} s^{-1}, a greatly reduced sheet resistance, and new quantum phenomena were obtained in the Nc-G single crystals.

RESULTS

Through the suppression of continuous nucleation during growth (figs. S2 and S3) (18, 19), an oxygen-assisted CVD strategy was designed to enable the growth of monolayer millimeter-sized Nc-G single

[1]Center for Nanochemistry, Beijing Science and Engineering Center for Nanocarbons, Beijing National Laboratory for Molecular Sciences, College of Chemistry and Molecular Engineering, Peking University, Beijing 100871, P. R. China. [2]Beijing Key Laboratory of Quantum Devices, Key Laboratory for the Physics and Chemistry of Nanodevices and Department of Electronics, Peking University, Beijing 100871, P. R. China. [3]China Fortune Land Development Industrial Investment Co. Ltd., Beijing, P. R. China; School of Economics and Management, Tsinghua University, Beijing, P. R. China. [4]Academy for Advanced Interdisciplinary Studies, Peking University, Beijing 100871, P. R. China. [5]State Key Laboratory of Precision Spectroscopy, School of Physics and Material Science, East China Normal University, Shanghai 200062, P. R. China. [6]Australian Institute for Bioengineering and Nanotechnology, The University of Queensland, Brisbane, QLD 4072, Australia. [7]Department of Materials Science and Engineering, College of Engineering, Peking University, Beijing 100871, P. R. China. [8]Soochow Institute for Energy and Materials Innovations, College of Physics, Optoelectronics and Energy, Collaborative Innovation Center of Suzhou Nano Science and Technology, Key Laboratory of Advanced Carbon Materials and Wearable Energy Technologies of Jiangsu Province, Soochow University, Suzhou 215006, P. R. China. [9]Center of Polymer and Carbon Materials, Polish Academy of Sciences, M. Curie-Sklodowskiej 34, Zabrze 41-819, Poland [10]Institute of Environmental Technology, VŠB–Technical University of Ostrava, 17. Listopadu 15, Ostrava 708 33, Czech Republic. [11]Center for Multidimensional Carbon Materials (CMCM), Institute for Basic Science (IBS), Ulsan 689-798, Republic of Korea. [12]School of Materials Science and Engineering, Ulsan National Institute of Science and Technology (UNIST), Ulsan 689-798, Republic of Korea. [13]Beijing Graphene Institute, Beijing 100095, P. R. China.
*These authors contributed equally to this work.
†Corresponding author. Email: zfliu@pku.edu.cn (Z.L.); hlpeng@pku.edu.cn (H.P.); f.ding@unist.ac.kr (F.D.); hqxu@pku.edu.cn (H.Q.X.)
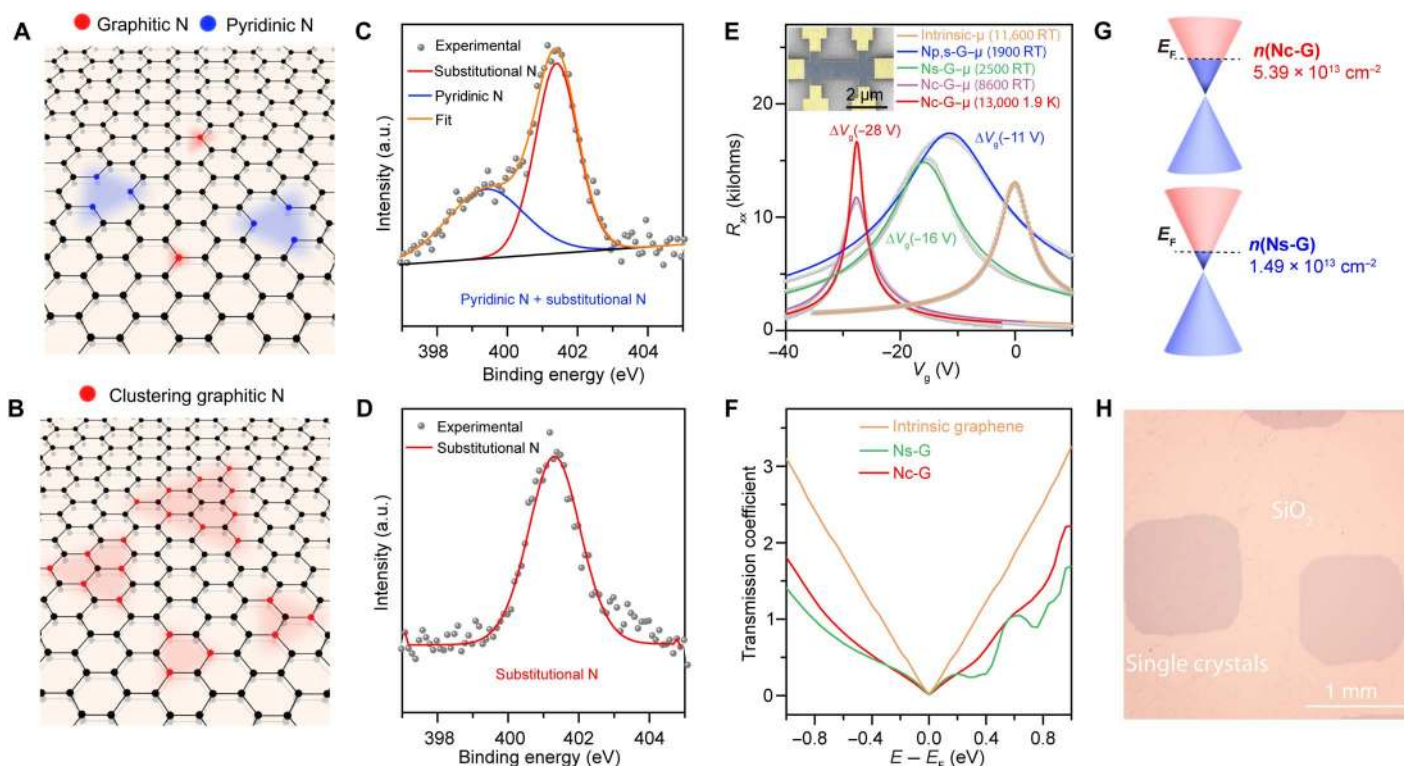
Fig. 1. Nc-G with millimeter-sized domains and record-breaking carrier mobility. (**A** and **B**) Schematics of the atomic structure of nitrogen-doped graphene, containing a mix of pyridinic N and graphitic N (A) and clusters with pure graphitic N (Nc-G) (B). (**C** and **D**) X-ray photoelectron spectroscopy (XPS) spectra of a nitrogen-doped graphene film grown by ACN, without (C) and with (D) the presence of surface oxygen during growth. The dopant concentration is calculated to be 1.4%. The peak around 399 eV is assigned to pyridinic nitrogen, and the peak at 401 eV is assigned to graphitic nitrogen. The area ratio of pyridinic nitrogen to the entire nitrogen is calculated to obtain the ratio of pyridinic nitrogen. Note that a hump (>402 eV) might be caused by physically absorbed NO and NO_2 or pyrolysis by-product of ACN. a.u., arbitrary units. (**E**) Typical plots of the resistance of intrinsic graphene (orange), graphene containing both pyridinic N and single-substitutional N (Np,s-G; blue), single-substitutional N (Ns-G; green) at room temperature (RT), Nc-G at room temperature (light purple), and 1.9 K (red) as a function of the gate voltage (V_g). Inset: False-colored scanning electron microscopy (SEM) image of the measured standard Hall bar device. (**F**) Calculated transmission coefficients of intrinsic graphene (orange), Ns-G (green), and Nc-G (red). The nitrogen concentration in graphene lattice is set to be 1.0% in Nc-G and Ns-G. (**G**) Calculated carrier concentration and Fermi level position of Nc-G (top) and Ns-G (bottom). (**H**) Optical microscopy image of millimeter-sized Nc-G single crystals transferred onto a SiO_2/Si substrate. The square domain shape of the Nc-G grains is mainly determined by the underlying oxygen-induced Cu(100) substrate, which would define the symmetry of graphene grains due to the carbon-metal interaction during the nucleation and epitaxial growth stage.

crystals (Fig. 1H), as confirmed by extensive transmission electron microscopy (TEM) and selected-area electron diffraction patterns (fig. S4). A conventional CVD growth process without the introduction of oxygen normally produces a nitrogen-doped graphene film containing observable pyridinic N along with substitutional N (Fig. 1C). However, our present strategy with oxygen assistance produces graphene film dominated by substitutional N (Fig. 1D), with a nitrogen concentration of 1.4% and with fine doping uniformity (fig. S5). These observations revealed that the presence of oxygen in the CVD process is responsible for the elimination/prevention of pyridinic nitrogen to achieve the substitutional doping. This can be understood by the selective etching of pyridinic nitrogen by forming N=O bonds and the subsequent removal of NO to yield a hexagonal lattice structure in graphene (20). The ^{13}C isotope–labeling method and Raman spectroscopy revealed a rapid growth rate of 160 μm min^{-1} (fig. S6) (21).

Compared to graphene containing both pyridinic N and single-substitutional N (Np,s-G) or only single-substitutional N (Ns-G) (2, 8, 22–28), the graphene film obtained in our work (Nc-G) exhibited a prominent enhancement of carrier mobility of ~8600 cm^2 V^{-1} s^{-1} at room temperature and 13,000 cm^2 V^{-1} s^{-1} at 1.9 K (using non-

linear fitting method) (Fig. 1E). We also observed a stronger n-doping effect in Nc-G than that in Ns-G and Np,s-G, as evident by a larger shift of Dirac point position in transfer curves relative to intrinsic counterpart. According to the equation $\sigma \sim n\mu e$, compared to the intrinsic counterpart (table S1), the enhanced carrier mobility and the stronger n-doping effect contribute to a greatly improved conductivity in Nc-G (detailed comparisons are listed in Table 1). Note that our synthesis method makes the conductivity of Nc-G improved, nearly 10 times in comparison with previously reported CVD-derived doped graphene (fig. S7) (2, 8, 13). Although several postgrowth doping approaches were also reported to enhance the conductivity of graphene, including molecule adsorption (6, 29, 30), metal doping (5, 31), and covalent modification (32), all of them still suffer from either poor stability or greatly reduced carrier mobility (table S2).

The enhanced carrier mobility and conductivity of Nc-G can be understood by following aspects: (i) Although the randomly distributed nitrogen dopants in Ns-G caused a significant scattering of carriers (11), such a scattering is significantly suppressed through the clusterization of nitrogen dopants (15). As shown in Fig. 1F, our theoretical calculations prove that the transmission coefficients of Nc-G are larger than

Table 1. Measured conductivity, carrier mobility, and Dirac point position values of graphene. RT, room temperature.

Doping configuration	Carrier mobility (cm^2 V^{-1} s^{-1})	Dirac point position (V)	Conductivity (S m^{-1})
Substitutional N+ pyridinic N	1900 (RT)	−11	9.30×10^5
Single-substitutional N	2500 (RT)	−16	1.96×10^6
Clustering substitutional N (1.4%)	**8600 (RT); 13,000 (1.9 K)**	**−28**	**1.62×10^7**
Clustering substitutional N (1.0%)	9900 (RT)	−17	8.41×10^6
Clustering substitutional N (0.6%)	11,000 (RT)	−8	6.10×10^6
Intrinsic graphene	11,600 (RT)	~0	7.29×10^5

that of Ns-G, demonstrating that the carriers in Nc-G would be subjected to a weaker scattering (higher transmission probability) when they propagate through potential barrier produced by dopants (*33*). (ii) A higher carrier concentration is found in Nc-G (5.39×10^{13} cm^{-2}) than that in Ns-G (1.49×10^{13} cm^{-2}). (Fig. 1G). Thus, the reduced carrier scattering and the enhanced carrier concentration would contribute to an enhanced conductivity.

We performed atomically resolved scanning tunneling microscopy (STM) imaging and density functional theory (DFT) calculations to explore the atomic structure of nitrogen atoms in the graphene lattice and the electronic structures of the Nc-G. Large-scale STM imaging revealed many bright areas with lateral sizes ranging from 2 to 6 nm, which were attributed to the graphitic nitrogen clusters in the hexagonal lattice (Fig. 2A and fig. S8). This stands in sharp contrast to the broadly observed single-substitutional dopant atoms observed in previous works (*34*) and our own results obtained using ammonia gas as the nitrogen source (fig. S9). The unique formation of graphitic nitrogen clusters might be understood by the dissociation products of ACN on the Cu(100) surface. Compared with NH$_3$, which can be dissociated into single N atoms only, the decomposition of an ACN molecule on the Cu(100) surface releases one carbon atom and a tightly bonded CN pair (fig. S10). The tightly bonded CN pairs on the Cu(100) surface contribute to the formation of carbon and nitrogen clusters. With respect to fast Fourier transform, we found two sets of hexagon reflexes. The inner hexagon arises from N-dopant–induced intervalley scattering and the outer hexagon corresponds to the graphene lattice (Fig. 2A, inset) (*34*). It can be seen that most nitrogen clusters had a threefold symmetry and the graphitic N atoms took up a triangular shape in the lattice. According to DFT calculations, the simulated STM images of 3N and 6N clusters match the experimental observations very well, which further verified the nitrogen cluster configuration (Fig. 2, B and C). On the basis of simulation results, the corresponding arrangement of nitrogen dopants is shown in Fig. 2D. The triangular-shaped nitrogen clusters are shown to have 3, 6, or 9 graphitic N atoms, respectively, separated by one or two neighboring C atoms in one doping center in a triangular shape. In addition, scanning tunneling spectroscopy (STS) observations confirm the n-type doping induced by the nitrogen clusters (fig. S11). Note that because of the relatively low nitrogen concentration and random distribution of nitrogen clusters in graphene lattice, the band structure of graphene is preserved, and only a shift of the Fermi level is observed.

The formation mechanism of triangular-shaped nitrogen clusters in the Nc-G films was explored by DFT calculations (*35*–*37*). The formation of magic C clusters on metal substrates has been studied,

and the most stable clusters were found to have a few pentagons (*37*). With the inclusion of N atoms, the stable C-N clusters showed quite different features. The theoretical calculations demonstrated that (i) all N atoms prefer the edge sites of a C-N cluster (figs. S12 and S13); (ii) contrary to the pure carbon clusters, C-N clusters with pentagons are less energetically favorable (fig. S14); and (iii) triangular-shaped C-N clusters with all N on the edge and all C in the centers are highly stable (fig. S15). On the basis of these features, we concluded that the most stable small C-N clusters on a Cu(100) surface are zigzag-edged triangles with N atoms at the edges (fig. S16). The most stable C-N clusters on the Cu(100) surface and their formation energies are shown in Fig. 2E, from which we can see that the exceptional stability of the N-edged triangular-shaped C-N clusters is confirmed by their very low formation energies in comparison with pure C clusters (2.6 to 3.15 eV versus 8 to 12 eV, respectively).

On the basis of the above theoretical analysis, a mechanism for the Nc-G film growth is shown in Fig. 2F. ACN molecules, with a stronger C≡N triple bond, are first adsorbed on the Cu(100) surface and then decompose into C atoms and C-N dimers; then, these precursors self-assemble into highly stable C-N clusters of various sizes on the Cu(100) surface at the high temperature of graphene growth. The mobility of a C-N cluster on the Cu(100) surface must be very low because its diffusion involves the motion of many atoms and, as a consequence, there will be many C-N clusters randomly distributed on the Cu(100) surface during CVD growth of graphene. Subsequently, with the propagation of the graphene front, the highly stable C-N clusters on the Cu(100) surface are gradually incorporated into the graphitic lattice and form in-plane triangular-shaped nitrogen clusters in the Nc-G film.

To further evaluate the electrical quality, we performed magneto-transport measurements on the Nc-G films transferred onto SiO$_2$/Si substrates. At a low temperature (1.9 K), the Nc-G films exhibit Shubnikov–de Haas oscillations of R_{xx} (Fig. 3A) and well-developed plateaus of R_{xy} (Fig. 3B), as a strong indicator of high quality of Nc-G. From a technological perspective, the tunability of the work function of graphene critically affects its industrial applications, especially regarding contact issues (*3*). In this regard, the growth temperature of N-doped graphene has been reported to influence the dopant concentration through temperature-dependent competition between the formation of C—C and C—N bonds (*26*). Here, we show that the tunability of work function of Nc-G films grown at different temperatures (see Materials and Methods) is approximately 300 meV using ultraviolet photo-electron spectroscopy (fig. S17A), which is consistent with our Raman
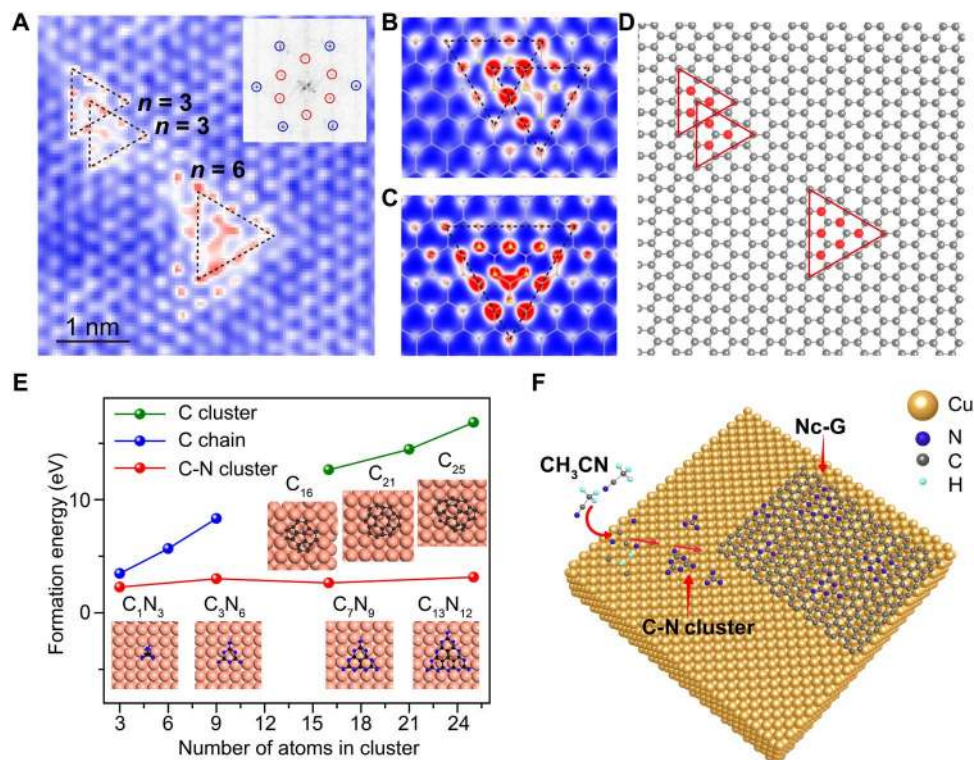
Fig. 2. The formation of nitrogen cluster. (**A**) Representative STM image of the clustered nitrogen atoms. The dashed triangles denote clusters with three or six nitrogen atoms. Inset: Corresponding fast Fourier transform of topography ($V_T = -0.002$ V and $I_T = 30.78$ nA). (**B** and **C**), Simulated STM images of two doping clusters with three nitrogen atoms (B) and one cluster with six nitrogen atoms (C). The yellow and gray balls denote nitrogen and carbon atoms, respectively. (**D**) Schematic of the atomic arrangement of in-plane clustered nitrogen dopants in graphene lattices based on simulation results. The red and gray balls denote nitrogen and carbon atoms, respectively. (**E**) Formation energy comparison between the triangular C-N clusters and pure carbon clusters. (**F**) Illustration of the Nc-G film formation. First, ACN molecules adsorb and decompose on the Cu(100) surface, forming precursors, such as C and N atoms and C-N groups (i). Then, these atoms and groups diffuse on the surface and assemble with each other, forming triangular-shaped C-N clusters (ii), and these clusters lastly incorporate into the lattice of the Nc-G film (iii).

spectroscopy studies, transport measurements, and x-ray photoelectron spectroscopy (XPS) investigations (fig. S17, B to E). The Nc-G exhibited a higher doping efficiency compared to Ns-G, which means that a higher work function tunability can be achieved in Nc-G with the same nitrogen concentration (fig. S17F). The tunability of work function, especially in the n-doping range, is crucial for graphene applications in solar cells and light-emitting diodes (3).

The nitrogen cluster doping provides a facile method to tune the work function of graphene and also enhances its conductivity, facilitating its application in optoelectronic devices including transparent electrodes and touch screens. We further experimentally observed the enhanced conductivity in our samples as indicated by a low sheet resistance of only ~130 ohms square^{-1} (Fig. 3C). Furthermore, our Nc-G film exhibited a transmittance of 97.7% at a wavelength of 550 nm according to ultraviolet-visible (UV-vis) transmittance spectroscopy measurements (fig. S18A). Large-scale evaluation of the conductivity of the Nc-G film, using a macroscopic four-probe method, still revealed a remarkably reduced sheet resistance as compared with that of pristine graphene without doping (fig. S18B). All these observations indicate that the as-grown Nc-G films are comparable to other transparent electrodes based on CVD-grown pristine graphene (38) and carbon nanotubes (39) (Fig. 3D). Wafer-scale Nc-G films were grown and transferred onto 4-inch SiO$_2$/Si wafers (Fig. 3D, inset), indicating the facile scalability of our method.

The large-area CVD-grown Nc-G film contained nitrogen dopant clusters embedded in the graphene lattice through strong covalent bonding, therefore demonstrating a high stability compared to unstable AuCl$_3$- and HNO$_3$-doped graphene films (5, 38), which both exhibit prominent reductions in conductivity after high-temperature processing (Fig. 3E). Furthermore, we fabricated multilayer graphene films using a layer-by-layer transfer method, leading to a clear improvement in the overall conductivity (fig. S18B). In a multilayer absorbent-doped graphene film, the chemical dopants in the lower layers of graphene are screened by the top layer and thus should display reduced doping effects, in contrast to the nearly constant doping effect observed in each individual layer of our multilayer Nc-G films. In a demonstration of the Nc-G film–based device, we integrated our Nc-G films into touch screen panels, for which the conductivity and transparency of electrodes are highly important, and rigorously tested in these devices (Fig. 3F, fig. S19, and movie S1).

Compared with previous methods, this graphitic nitrogen cluster doping technique has the advantage of producing highly positively charged impurities in graphene, which would also result in rich quantum transport phenomena. An interesting transport feature in the transfer curves of Nc-G samples is that the resistance exhibits well-resolved and pronounced oscillations near the Dirac point region (Fig. 4A, inset). To investigate the oscillatory part of resistance further, we subtract a slowly varying polynomial background resistance. In
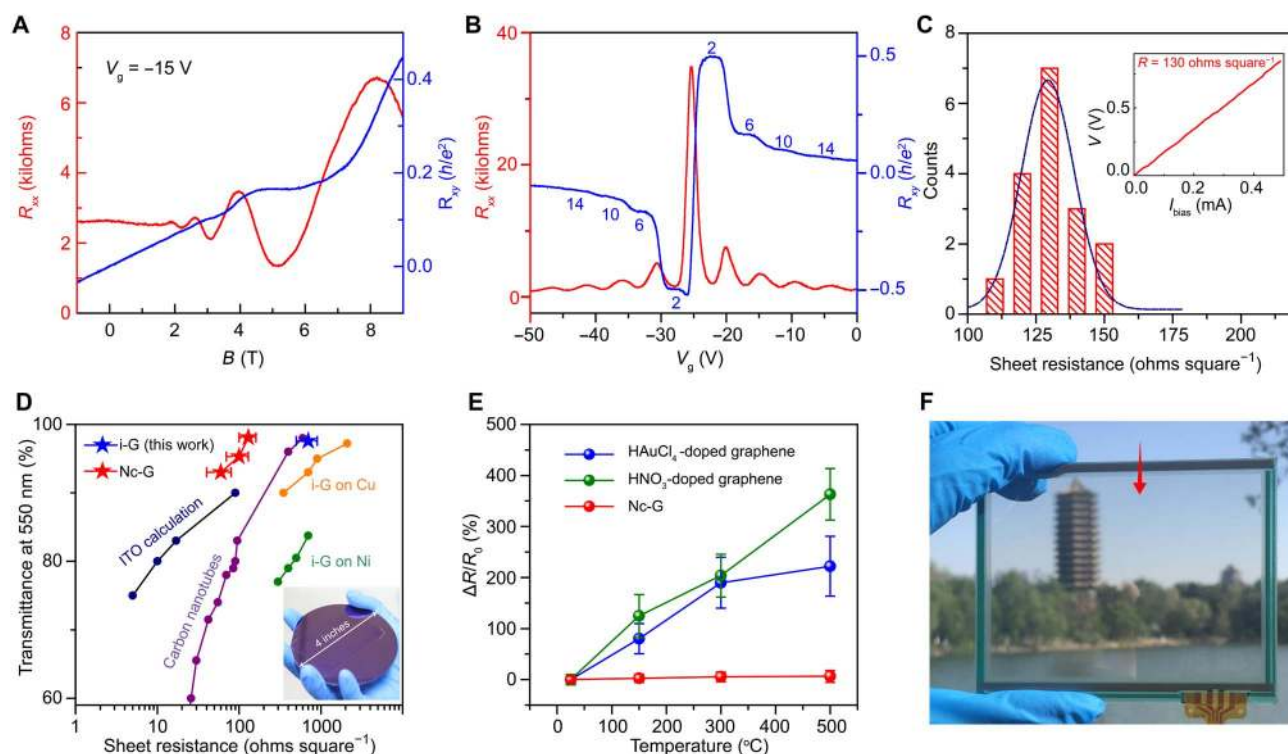
Fig. 3. Electrical properties of Nc-G film. (**A**) Typical plot of the longitudinal resistance (R_{xx}, red) and Hall resistance (R_{xy}, blue) a function of the magnetic field measured at a fixed gate voltage (−15 V). (**B**) Plot of the R_{xx} (red) and R_{xy} (blue) as a function of the gate voltage measured at 1.9 K and a magnetic field of 4 T. (**C**) Sheet resistance statistics of the Nc-G film. Inset: Representative I-V curve using a four-probe measurement. (**D**) Sheet resistance versus optical transmission (at 550 nm) for the monolayer, bilayer, and trilayer Nc-G films and a pristine graphene film (i-G) with ~1-mm domain size for contrast. The performances of pristine graphene grown on copper and nickel (38) and carbon nanotubes (39) are shown for comparison. Inset: Contrast-enhanced photograph of the wafer-sized, continuous Nc-G film on a 4-inch SiO_2/Si substrate. (**E**) Changes in the sheet resistance of the as-synthesized Nc-G film, HNO_3-doped graphene film, and $HAuCl_4$-doped graphene film under high-temperature treatment. (**F**) A photograph showing Weiming Lake and Boya Tower at Peking University seen through a touch screen device with a graphene/polyethylene terephthalate electrode. A movie showing the operation of the device is provided in movie S1. (Photo credits: Li Lin, Peking University).

Fig. 4A, we show the subtracted differential resistance as a function of gate voltage (V_g) for selected magnetic fields measured at 1.9 K, where each trace exhibits a clear oscillation as a function of V_g. The structure of oscillations is more visible when the resistance is plotted as a function of the magnetic field and gate voltage. The positions of the resistance peaks evolve almost linearly with B, giving rise to sets of parallel lines in the B-V_g plane (Fig. 4B). In contrast, we observed no resistance oscillations in pristine graphene with zero nitrogen doping, suggesting that the nitrogen cluster doping lies behind the observed resistance oscillations. Recently, theoretical calculations have predicted that highly charged impurities in graphene could lead to the production of a strong Coulomb potential and the formation of quasi-bound states (40–42). The strong coupling of these quasi-bound states to the massless carriers also leads to resonance scattering near the cluster-doped N atoms, resulting in a series of oscillatory dependence of the electrical conductivity on the carrier density (40). Our theoretical calculations confirmed that there exists a higher electrostatic potential near the nitrogen cluster doping center than that found at a single-substitutional doping center (Fig. 4C). Consequently, quasi-bound states appear near the Fermi-level of 6N cluster– and 3N cluster–doped graphene, as evidenced by a strong enhancement of the density of states (Fig. 4D and fig. S20). In contrast, no obvious quasi-bound state is observed near the Fermi-level of single substitutional doped graphene (Fig. 4E). The emergence of these quasi-bound states,

together with the observed oscillating resistance as a function of carrier density, further confirms the presence of nitrogen clusters in graphene lattice. Furthermore, the highly charged impurities in the nitrogen-clustering region ideally produce an atomic-scale circular graphene p-n junction approaching the few-nanometer limit, along with an extraordinarily high work function difference. This may provide an ideal platform for realizing electron optics by enabling the switching and guiding of electrons (43, 44). On the other hand, the existence of clustering nitrogen would strongly break the inversion symmetry of graphene lattice, which can be used for the investigation of the spin and valley states in strong quantum confinement regions.

DISCUSSION
Our findings here suggest that the clusterization of dopants in graphene would significantly reduce carrier scattering by dopants, and simultaneously enhance carrier concentration. These should promote further exploration studies of high mobility/conductivity in other 2D materials. As we achieve scalable production of Nc-G films, their high mobility/conductivity and tunable work function, as well as high stability, make Nc-G films a promising material for the realization of novel quantum phenomena, future high-speed chips, and flexible electronics applications, where high mobility/conductivity is highly required. Furthermore, in Nc-G, the positive charges on adjacent carbon atoms in
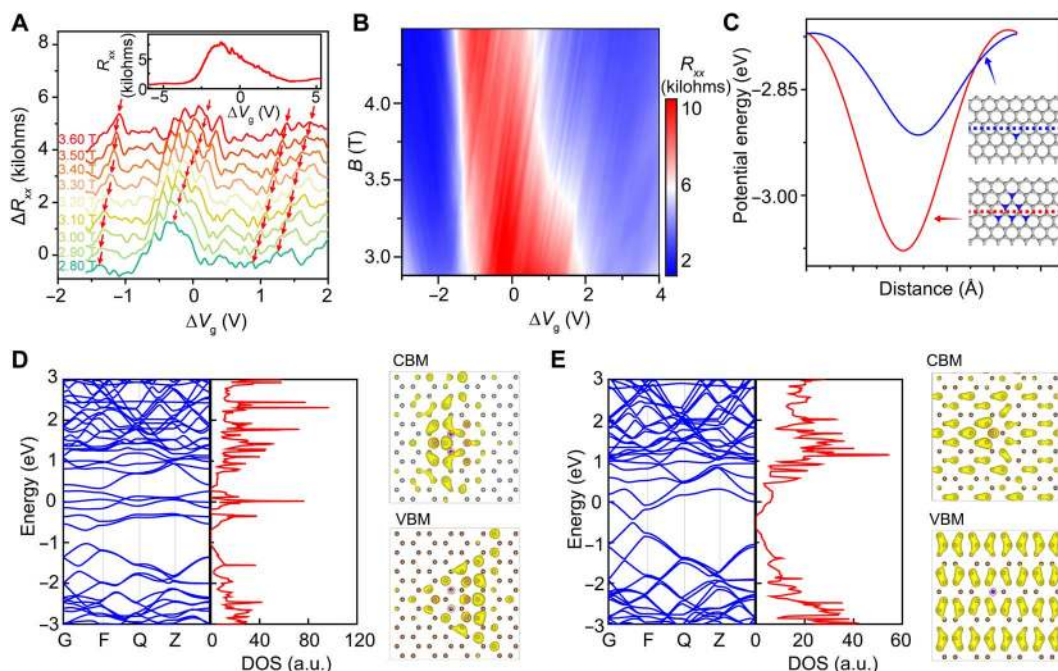
Fig. 4. Resistance oscillations in Nc-G film. (A) ΔR_{xx} of the sample with the 1.4% N atomic concentration as a function of gate voltage taken at several constant magnetic fields and $T = 1.9$ K, obtained by subtracting a smooth background. The curves are shifted vertically for clarity. Inset: Typical transfer curve of nitrogen-doped graphene samples, showing pronounced oscillations near the Dirac point. **(B)** Color scale plot of the R_{xx} as a function of gate voltage and magnetic field, showing an oscillatory pattern near the Dirac point region. **(C)** The electrostatic potential of 6N cluster–doped graphene (red) and single N atom–doped graphene (blue). Inset: Corresponding schematics of the atomic structure of 6N cluster–doped graphene and single N atom–doped graphene. **(D and E)** Energy bandgap, density of states (DOS), and the partial charge distribution of valance band maximum (VBM) and conducting band minimum (CBM) of 6N cluster–doped graphene **(D)** and single N atom–doped graphene **(E)**.

each doping center would be further enhanced, which endow Nc-G with enhanced catalytic ability as nonmetallic catalysis.

MATERIALS AND METHODS
The growth procedure for Nc-G film
Pretreatment
Commercially available Cu foil (#46365, Alfa Aesar) was electrochemically polished, using a solution of phosphoric acid and ethylene glycol (volume ratio of 3:1) to clean the surface. After polishing, the Cu foil was loaded into a low-pressure CVD system equipped with a 1-inch-diameter quartz tube. The nitrogen-containing carbon source, liquid ACN with a partial vapor pressure of ~1 Pa, was introduced into the system to grow Nc-G. Note that ACN was introduced into the CVD chamber by the evaporation of ACN at low pressure. In addition, a metering valve (SS-SS4, Swagelok) was used to adjust the flow rate of ACN, which was held constant to ensure uniform doping during the growth.

A diagram of the temperature profile adopted was shown in fig. S1. The growth system was first rapidly heated to 1020°C, under H_2 with a flow rate of 100 cm^3 min^{-1} (sccm) (60 Pa) as background gas to create a reducing environment. The Cu foil was annealed for an additional hour to reduce surface oxide and increase the Cu grain size. After the annealing step, the reducing gas was totally shut off so that oxygen with a flow rate of 0.2 sccm (0.5 Pa) could be introduced to suppress nucleation. In more detail, the introduction of oxygen passivates the active sites for graphene nucleation on the Cu foil, which

has proved to be efficient for growing centimeter-sized single-crystal graphene.

First nucleation
After oxygen pretreatment, the temperature was reduced to 900°C (for the case of growing the sample denoted as 900 Nc-G). The first nucleation of Nc-G on Cu foil was initiated by introducing ACN vapor under a H_2 flow of 100 sccm (61 Pa). In our case, a partial pressure of ~1 Pa of ACN was held during the growth to precisely control the doping level. However, the nucleation density was rather high, although oxygen pretreatment had been carried out. The as-synthesized NG grains exhibited a broad distribution of domain sizes, indicating that the grains were not formed at the same time. It was found that 5 min of injecting ACN was sufficient to produce Nc-G nucleation with a maximum domain size of 100 μm.

Oxygen-assisted etching
After the first nucleation of Nc-G, the ACN and the reducing gas were completely shut off, and oxygen with a flow rate of 0.2 sccm (0.5 Pa) was subsequently introduced to initiate etching of the Nc-G nuclei that had been formed. The duration of the etching process was no more than 2 min, determined by the maximum domain size of the as-formed grains.

Regrowth
ACN and hydrogen were subsequently reintroduced into the CVD system to restart the growth of Nc-G, using with same flow rates to ensure an unchanged doping level for the regrowth step. After around 10-min growth, Nc-G grains with millimeter domain sizes were synthesized. Note that around 1 hour of growth was certainly sufficient to

achieve full coverage of Nc-G on the Cu foil. After the growth, the ACN and reducing hydrogen flows were left unchanged, and the sample was quickly cooled to 700°C over 2 min and then reaching room temperature in 20 min. Note that additional growth-etching-regrowth cycles could be carried out by repeating the nucleation and passivation steps for further suppression of nucleation.

Graphene transfer

To minimize the presence of transfer-related charge impurities, individual Nc-G domains or continuous films were transferred onto SiO₂/Si substrates using a polymethyl methacrylate (PMMA)–assisted "dry" method; these samples were used for Raman spectroscopy characterizations and electrical device fabrication. The graphene was grown on both sides of the Cu foils, and one side of the graphene, to be used for characterization, was spin-coated with PMMA and baked at 150°C for 5 min. The other side of the sample was then exposed to O₂ plasma for 3 min to remove the graphene, followed by application of 1 M $Na_2S_2O_8$ solution to etch the Cu away. The free-standing PMMA/graphene membrane floating on the surface of the etching solution was washed three times with deionized water. After being rinsed with deionized water, the PMMA/graphene was subsequently washed with isopropanol and dried in air for 12 hours before being placed onto the target substrate. Subsequently, the graphene became directly attached to the SiO₂/Si substrate through heating the substrate to 150°C. To minimize transfer-related impurities, the films were further heated to 150°C for 1 hour before removing the polymer. The PMMA was removed by dissolving with acetone, yielding graphene Nc-G domains or continuous films on the substrate.

Transport property measurements

The graphene samples were transferred onto SiO₂/Si substrates with marks for alignments and then subjected to heat cleaning and atomic force microscopy (AFM) (Veeco Dimension 3100) imaging to determine whether they were flat. Next, each graphene sample was etched into a Hall bar geometry using a PMMA etching mask (PMMA 950 K A2 at 4000 rpm) designed by electron beam lithography (EBL) (Raith 150 2nd) and reactive-ion etching with O₂ (Trion Technology Minilock III). After the samples were patterned, additional AFM imaging was performed to ensure that the channel regions were free of wrinkles and residues. Last, after using EBL to design a PMMA mask (PMMA 950 K A4 at 4000 rpm), 5-nm Ti and 90-nm Au were deposited on the samples using an electron-beam evaporator (Kurte J. Lesker AXXIS) and then a standard metal lift-off technique.

Electrical characterization at room temperature was performed in a vacuum probe station (Lakeshore TTP-4) using a Keithley Semiconductor Characterization System (Model 4200-SCS). Electrical-transport and magnetotransport measurements at low temperatures were performed using a lock-in amplifier (Stanford Research 830) at 17 Hz with a source current of 10 to 100 nA.

STM/STS measurements

An Omicron VT-STM/STS system was used for STM characterization and STS measurements. All the STM data were obtained under constant current mode with the sample holder at room temperature. The STS local differential conductance (dI/dV) spectra were measured at 77 K by recording the output of a lock-in system with a manually disabled feedback loop. A modulation signal of 5 mV and 932 Hz was selected under a tunneling condition of 1 V and 20 pA.

Characterization

The morphology and structure of the as-grown Nc-G film or continuous film on Cu foil or a dielectric substrate were characterized by optical microscopy (BX51, Olympus), scanning electron microscopy (SEM) (S-4800, Hitachi; acceleration voltage, 5 to 30 kV), and Raman spectroscopy (LabRAM HR-800, HORIBA; 514-nm laser, 100× objective). Optical transmittance spectra were collected on a PerkinElmer LAMBDA 950 UV-vis spectrophotometer. The graphene domains on the amorphous carbon–covered TEM grid were characterized by TEM (FEI Tecnai T20; acceleration voltage, 200 kV). Aberration-corrected TEM studies were performed using an FEI 80-300 environmental Titan operated in monochromatic mode at 80 kV. The elemental analysis of the as-synthesized Nc-G films was performed using XPS (Kratos Analytical AXIS Ultra with monochromatic Al-Kα irradiation). The large-scale sheet resistances of the films were characterized using a four-probe resistance measuring meter (RTS-4, Guangzhou 4-Probe Tech Co. Ltd.) based on a four-point probe method to eliminate the contact resistance. Four metal probes were aligned in a line with intervals of 1 mm.

DFT calculations

All the calculations were performed within the framework of DFT as implemented in the Vienna ab initio simulation package (VASP). Electronic exchange and correlation were included by the generalized gradient approximation (GGA) in the Perdew-Burke-Ernzerhof functional. The interactions between the valence electrons and ion cores were described by the projected augmented wave method, and the energy cutoff for the plane wave functions was 400 eV. All structures were optimized until the maximum force component on each atom was less than 0.02 eV Å⁻¹. The vacuum layer inside the super cell was larger than 10 Å to avoid the interaction of the adjacent unit cell. The Cu(100) substrate was represented by an ABC-stacked four-layer slab model, with the bottom layer fixed to mimic the bulk Cu atoms. The slab model was composed of 5 × 5, 6 × 6, and 7 × 7 repeating unit cells based on the size of the carbon-nitrogen (C-N) cluster, and a 1 × 1 × 1 k-point mesh was used for the calculations. STM images were calculated within the Tersoff-Hamman approximation.

The formation energy, E_f, of a C-N cluster on the surface was calculated by

$$E_f = E(Cu - C_nN_m) - n \times E(C \text{ in } G) - (m/2) \times E(N_2) - E(Cu) \qquad (1)$$

where $E(Cu - C_nN_m)$ is the total energy of the C_nN_m cluster adsorbed on the Cu(100) substrate and n and m are the numbers of C and N atoms in the C-N cluster, respectively. $E(C \text{ in } G)$ is the energy of a C atom in graphene, $E(N_2)$ is the energy of a nitrogen molecule, and $E(Cu)$ is the energy of the Cu(100) substrate.

The formation energy, E_f, of a carbon cluster on the surface was calculated by

$$E_f = E(Cu - C_n) - n \times E(C \text{ in } G) - E(Cu) \qquad (2)$$

where $E(Cu - C_n)$ is the total energy of the C_n cluster adsorbed on the Cu(100) substrate and n is the number of C atoms in the carbon cluster; $E(C \text{ in } G)$ is the energy of a C atom in graphene, and $E(Cu)$ is the energy of the Cu(100) substrate.

Transmission coefficients were calculated using a two-probe setup by DFT within the Keldysh nonequilibrium Green's function formalism as implemented in Nanodcal. The transmission coefficients are defined as the average of transmission over all transverse k-points.

A linear combination of atomic orbital basis at the double-ζ polarization level was used. The energy cutoff for the real-space grid is taken at 80 Hartree, which is a quite safe energy for graphene. GGA was used for the exchange-correlation potential. Transport is along the x direction, and the devices are periodic along the y direction. k-points ($1 \times 5 \times 1$ and $1 \times 100 \times 1$) were used to sample the Brillouin zone in the self-consistent loop and the transmission calculations, respectively. Convergence was achieved when the total energy, every element of the Hamiltonian, and density matrices change less than $5 \times e^{-5}$ arbitrary units during adjacent self-consistent runs.

The carrier densities calculated in Nanodcal can be written as

$$n = \int_{E_f}^{\infty} g_c(E) f(E - \mu) d(E)$$
$$p = \int_{-\infty}^{E_f} g_v(E) [1 - f(E - \mu)] d(E)$$

where $g(E)$ is the density of states, $f(E)$ is the Fermi-Dirac probability function, and μ is the chemical potential energy. In this work, the carrier densities were calculated using a chemical potential energy of 0.1 eV.

All the doped structures used for the transmission coefficient and carrier density calculations are relaxed using VASP. The left and right leads are ideal graphene with buffer layers added in the central scattering region.

SUPPLEMENTARY MATERIALS

Supplementary material for this article is available at http://advances.sciencemag.org/cgi/content/full/5/8/eaaw8337/DC1

Supplementary Method

Fig. S1. Procedure for the growth of Nc-G films.
Fig. S2. The continuous nucleation of nitrogen-doped graphene.
Fig. S3. The effect of the oxygen-assisted etching-regrowth cycle on suppression of nucleation.
Fig. S4. Structural characterization of as-grown large Nc-G single crystals.
Fig. S5. Raman characterizations of Nc-G grains.
Fig. S6. The isotopic labeling experiment to visualize the growth kinetics of millimeter-sized Nc-G grains.
Fig. S7. The reported $n\mu$ and σ values function as μ in Nc-G of this work (red) and previous CVD doping strategies (navy blue).
Fig. S8. STM images of the clustered nitrogen dopants in graphene lattice.
Fig. S9. The STM and STS characterization of single-substitutional nitrogen-doped graphene.
Fig. S10. Calculated dissociation energy of C-C-N.
Fig. S11. STS measurements of Nc-G films.
Fig. S12. N atoms prefer to stay on the edge of a C-N cluster.
Fig. S13. C-N clusters without N atoms at the center are more stable.
Fig. S14. C-N cluster with flat structure is more stable.
Fig. S15. C-N cluster with high ratio of N atoms at the edge is more stable.
Fig. S16. A series of triangular shaped C-N clusters with N edges have very low formation energies.
Fig. S17. The doping efficiency of Nc-G film.
Fig. S18. The large-scale conductivity and transmittance of Nc-G films.
Fig. S19. Potential application of Nc-G films.
Fig. S20. High electrostatic potential and quasi-bound states induced by nitrogen clusters.
Movie S1. Demonstration of a flexible touch screen device made from Nc-G film.
Table S1. Mobilities and sheet resistance of previously reported intrinsic graphene.
Table S2. Mobilities, conductivity, and stability of previously reported doped graphene.
References (45–62)

REFERENCES AND NOTES

1. X. Wang, X. Li, L. Zhang, Y. Yoon, P. K. Weber, H. Wang, J. Guo, H. Dai, N-doping of graphene through electrothermal reactions with ammonia. *Science* **324**, 768–771 (2009).

2. D. Wei, Y. Liu, Y. Wang, H. Zhang, L. Huang, G. Yu, Synthesis of N-doped graphene by chemical vapor deposition and its electrical properties. *Nano Lett.* **9**, 1752–1758 (2009).

3. K. S. Novoselov, V. I. Fal'ko, L. Colombo, P. R. Gellert, M. G. Schwab, K. Kim, A roadmap for graphene. *Nature* **490**, 192–200 (2012).

4. A. C. Ferrari, F. Bonaccorso, V. Fal'ko, K. S. Novoselov, S. Roche, P. Bøggild, S. Borini, F. H. L. Koppens, V. Palermo, N. Pugno, J. A. Garrido, R. Sordan, A. Bianco, L. Ballerini, M. Prato, E. Lidorikis, J. Kivioja, C. Marinelli, T. Ryhänen, A. Morpurgo, J. N. Coleman, V. Nicolosi, L. Colombo, A. Fert, M. Garcia-Hernandez, A. Bachtold, G. F. Schneider, F. Guinea, C. Dekker, M. Barbone, Z. Sun, C. Galiotis, A. N. Grigorenko, G. Konstantatos, A. Kis, M. Katsnelson, L. Vandersypen, A. Loiseau, V. Morandi, D. Neumaier, E. Treossi, V. Pellegrini, M. Polini, A. Tredicucci, G. M. Williams, B. Hee Hong, J.-H. Ahn, J. Min Kim, H. Zirath, B. J. van Wees, H. van der Zant, L. Occhipinti, A. di Matteo, I. A. Kinloch, T. Seyller, E. Quesnel, X. Feng, K. Teo, N. Rupesinghe, P. Hakonen, S. R. T. Neil, Q. Tannock, T. Löfwander, J. Kinaret, Science and technology roadmap for graphene, related two-dimensional crystals, and hybrid systems. *Nanoscale* **7**, 4598–4810 (2015).

5. Y. Shi, K. K. Kim, A. Reina, M. Hofmann, L.-J. Li, J. Kong, Work function engineering of graphene electrode via chemical doping. *ACS Nano* **4**, 2689–2694 (2010).

6. T. Lohmann, K. von Klitzing, J. H. Smet, Four-terminal magneto-transport in graphene p-n junctions created by spatially selective doping. *Nano Lett.* **9**, 1973–1979 (2009).

7. A. Das, S. Pisana, B. Chakraborty, S. Piscanec, S. K. Saha, U. V. Waghmare, K. S. Novoselov, H. R. Krishnamurthy, A. K. Geim, A. C. Ferrari, A. K. Sood, Monitoring dopants by Raman scattering in an electrochemically top-gated graphene transistor. *Nat. Nanotechnol.* **3**, 210–215 (2008).

8. Z. Sun, Z. Yan, J. Yao, E. Beitler, Y. Zhu, J. M. Tour, Growth of graphene from solid carbon sources. *Nature* **468**, 549–552 (2010).

9. D. Usachov, O. Vilkov, A. Grüneis, D. Haberer, A. Fedorov, V. K. Adamchuk, A. B. Preobrajenski, P. Dudin, A. Barinov, M. Oehzelt, C. Laubschat, D. V. Vyalikh, Nitrogen-doped graphene: Efficient growth, structure, and electronic properties. *Nano Lett.* **11**, 5401–5407 (2011).

10. L. Qu, Y. Liu, J. B. Beak, L. Dai, Nitrogen-doped graphene as efficient metal-free electrocatalyst for oxygen reduction in fuel cells. *ACS Nano* **4**, 1321–1326 (2010).

11. A. Lherbier, X. Blase, Y.-M. Niquet, F. Triozon, S. Roche, Charge transport in chemically doped 2D graphene. *Phys. Rev. Lett.* **101**, 036808 (2008).

12. H. Liu, Y. Liu, D. Zhu, Chemical doping of graphene. *J. Mater. Chem.* **21**, 3335–3345 (2011).

13. S. De, J. N. Coleman, Are there fundamental limitations on the sheet resistance and transmittance of thin graphene films? *ACS Nano* **4**, 2713–2720 (2010).

14. T. Schiros, D. Nordlund, L. Pálová, D. Prezzi, L. Zhao, K. S. Kim, U. Wurstbauer, C. Gutiérrez, D. Delongchamp, C. Jaye, D. Fischer, H. Ogasawara, L. G. M. Pettersson, D. R. Reichman, P. Kim, M. S. Hybertsen, A. N. Pasupathy, Connecting dopant bond type with electronic structure in N-doped graphene. *Nano Lett.* **12**, 4025–4031 (2012).

15. M. Katsnelson, F. Guinea, A. K. Geim, Scattering of electrons in graphene by clusters of impurities. *Phys. Rev. B* **79**, 195426 (2009).

16. J. Yu, C.-H. Lee, D. Bouilly, M. Han, P. Kim, M. L. Steigerwald, X. Roy, C. Nuckolls, Patterning superatom dopants on transition metal dichalcogenides. *Nano Lett.* **16**, 3385–3389 (2016).

17. Q. Yu, L. A. Jauregui, W. Wu, R. Colby, J. Tian, Z. Su, H. Cao, Z. Liu, D. Pandey, D. Wei, T. F. Chung, P. Peng, N. P. Guisinger, E. A. Stach, J. Bao, S.-S. Pei, Y. P. Chen, Control and characterization of individual grains and grain boundaries in graphene grown by chemical vapour deposition. *Nat. Mater.* **10**, 443–449 (2011).

18. L. Lin, L. Sun, J. Zhang, J. Sun, A. L. Koh, H. Peng, Z. Liu, Rapid growth of large single crystalline graphene via second passivation and multistage carbon supply. *Adv. Mater.* **28**, 4671–4677 (2016).

19. Y. Hao, M. S. Bharathi, L. Wang, Y. Liu, H. Chen, S. Nie, X. Wang, H. Chou, C. Tan, B. Fallahazad, H. Ramanarayan, C. W. Magnuson, E. Tutuc, B. I. Yakobson, K. F. McCarty, Y.-W. Zhang, P. Kim, J. Hone, L. Colombo, R. S. Ruoff, The role of surface oxygen in the growth of large single-crystal graphene on copper. *Science* **342**, 720–723 (2013).

20. W. Wei, Z. Wei, S. Chen, X. Qi, T. Yang, J. Hu, D. Wang, L. J. Wan, S. F. Alvi, L. Li, Space-confinement-induced synthesis of pyridinic- and pyrrolic-nitrogen-doped graphene for the catalysis of oxygen reduction. *Angew. Chem. Int. Ed.* **52**, 11755–11759 (2013).

21. X. Li, W. Cai, L. Colombo, R. S. Ruoff, Evolution of graphene growth on Ni and Cu by carbon isotope labeling. *Nano Lett.* **9**, 4268–4272 (2009).

22. Y. Xue, B. Wu, L. Jiang, Y. Guo, L.-J. Huang, J. Chen, J. Tan, D. Geng, B. Luo, W. Hu, G. Yu, Y. Liu, Low temperature growth of highly nitrogen-doped single crystal graphene arrays by chemical vapor deposition. *J. Am. Chem. Soc.* **134**, 11060–11063 (2012).

23. J. Zhang, J. Li, Z. Wang, X. Wang, W. Feng, W. Zheng, W. Cao, P. A. Hu, Low-temperature growth of large-area heteroatom-doped graphene film. *Chem. Mater.* **26**, 2460–2466 (2014).

24. Y.-F. Lu, S.-T. Lo, J.-C. Lin, W. Zhang, J.-Y. Lu, F.-H. Liu, C.-M. Tseng, Y.-H. Lee, C.-T. Liang, L.-J. Li, Nitrogen-doped graphene sheets grown by chemical vapor deposition: Synthesis

and influence of nitrogen impurities on carrier transport. *ACS Nano* **7**, 6522–6532 (2013).

25. H. C. Wu, M. Abid, Y. C. Wu, C. Ó Coileáin, A. Syrlybekov, J. F. Han, C. L. Heng, H. Liu, M. Abid, I. Shvets, Enhanced Shubnikov–de Haas oscillation in nitrogen-doped graphene. *ACS Nano* **9**, 7207–7214 (2015).

26. B. He, Z. Ren, C. Qi, S. Yan, Z. Wang, Synthesis of nitrogen-doped monolayer graphene with high transparent and n-type electrical properties. *J. Mater. Chem. C* **3**, 6172–6177 (2015).

27. Z. Wang, P. Li, Y. Chen, J. Liu, H. Tian, J. Zhou, W. Zhang, Y. Li, Synthesis of nitrogen-doped graphene by chemical vapour deposition using melamine as the sole solid source of carbon and nitrogen. *J. Mater. Chem. C* **2**, 7396–7401 (2014).

28. H. Gao, L. Song, W. Guo, L. Huang, D. Yang, F. Wang, Y. Zuo, X. Fan, Z. Liu, W. Gao, R. Vajtai, K. Hackenberg, P. M. Ajayan, A simple method to synthesize continuous large area nitrogen-doped graphene. *Carbon* **50**, 4476–4482 (2012).

29. P.-H. Ho, Y.-C. Yeh, D.-Y. Wang, S.-S. Li, H.-A. Chen, Y.-H. Chung, C.-C. Lin, W.-H. Wang, C.-W. Chen, Self-encapsulated doping of n-type graphene transistors with extended air stability. *ACS Nano* **6**, 6215–6221 (2012).

30. F. Schedin, A. K. Geim, S. V. Morozov, E. W. Hill, P. Blake, M. I. Katsnelson, K. S. Novoselov, Detection of individual gas molecules adsorbed on graphene. *Nat. Mater.* **6**, 652–655 (2007).

31. K. M. McCreary, K. Pi, A. G. Swartz, W. Han, W. Bao, C. N. Lau, F. Guinea, M. I. Katsnelson, R. K. Kawakami, Effect of cluster formation on graphene mobility. *Phys. Rev. B* **81**, 115453 (2010).

32. D. C. Elias, R. R. Nair, T. M. G. Mohiuddin, S. V. Morozov, P. Blake, M. P. Halsall, A. C. Ferrari, D. W. Boukhvalov, M. I. Katsnelson, A. K. Geim, K. S. Novoselov, Control of graphene's properties by reversible hydrogenation: Evidence for graphane. *Science* **323**, 610–613 (2009).

33. M. Katsnelson, K. Novoselov, A. Geim, Chiral tunnelling and the Klein paradox in graphene. *Nat. Phys.* **2**, 620–625 (2006).

34. L. Zhao, R. He, K. T. Rim, T. Schiros, K. S. Kim, H. Zhou, C. Gutiérrez, S. P. Chockalingam, C. J. Arguello, L. Pálová, D. Nordlund, M. S. Hybertsen, D. R. Reichman, T. F. Heinz, P. Kim, A. Pinczuk, G. W. Flynn, A. N. Pasupathy, Visualizing individual nitrogen dopants in monolayer graphene. *Science* **333**, 999–1003 (2011).

35. B. Wang, X. Ma, M. Caffio, R. Schaub, W.-X. Li, Size-selective carbon nanoclusters as precursors to the growth of epitaxial graphene. *Nano Lett.* **11**, 424–430 (2011).

36. Y. Cui, Q. Fu, H. Zhang, X. Bao, Formation of identical-size graphene nanoclusters on Ru(0001). *Chem. Commun.* **47**, 1470–1472 (2011).

37. Q. Yuan, J. Gao, H. Shu, J. Zhao, X. Chen, F. Ding, Magic carbon clusters in the chemical vapor deposition growth of graphene. *J. Am. Chem. Soc.* **134**, 2970–2975 (2011).

38. S. Bae, H. Kim, Y. Lee, X. Xu, J. S. Park, Y. Zheng, J. Balakrishnan, T. Lei, H. Ri Kim, Y. I. Song, Y. J. Kim, K. S. Kim, B. Özyilmaz, J. H. Ahn, B. H. Hong, S. Iijima, Roll-to-roll production of 30-inch graphene films for transparent electrodes. *Nat. Nanotechnol.* **5**, 574–578 (2010).

39. H.-Z. Geng, K. K. Kim, K. P. So, Y. S. Lee, Y. Chang, Y. H. Lee, Effect of acid treatment on carbon nanotube-based flexible transparent conducting films. *J. Am. Chem. Soc.* **129**, 7758–7759 (2007).

40. A. Shytov, M. Katsnelson, L. Levitov, Atomic collapse and quasi–Rydberg states in graphene. *Phys. Rev. Lett.* **99**, 246802 (2007).

41. Y. Wang, D. Wong, A. V. Shytov, V. W. Brar, S. Choi, Q. Wu, H.-Z. Tsai, W. Regan, A. Zettl, R. K. Kawakami, S. G. Louie, L. S. Levitov, M. F. Crommie, Observing atomic collapse resonances in artificial nuclei on graphene. *Science* **340**, 734–737 (2013).

42. J. Mao, Y. Jiang, D. Moldovan, G. Li, K. Watanabe, T. Taniguchi, M. R. Masir, F. M. Peeters, E. Y. Andrei, Realization of a tunable artificial atom at a supercritically charged vacancy in graphene. *Nat. Phys.* **12**, 545–549 (2016).

43. Y. Jiang, J. Mao, D. Moldovan, M. R. Masir, G. Li, K. Watanabe, T. Taniguchi, F. M. Peeters, E. Y. Andrei, Tuning a circular p-n junction in graphene from quantum confinement to optical guiding. *Nat. Nanotechnol.* **12**, 1045–1049 (2017).

44. S. Chen, Z. Han, M. M. Elahi, K. M. M. Habib, L. Wang, B. Wen, Y. Gao, T. Taniguchi, K. Watanabe, J. Hone, A. W. Ghosh, C. R. Dean, Electron optics with p-n junctions in ballistic graphene. *Science* **353**, 1522–1525 (2016).

45. G. H. Han, F. Güneş, J. J. Bae, E. S. Kim, S. J. Chae, H.-J. Shin, J.-Y. Choi, D. Pribat, Y. H. Lee, Influence of copper morphology in forming nucleation seeds for graphene growth. *Nano Lett.* **11**, 4144–4148 (2011).

46. L. Lin, J. Li, H. Ren, A. L. Koh, N. Kang, H. Peng, H. Q. Xu, Z. Liu, Surface engineering of copper foils for growing centimeter-sized single-crystalline graphene. *ACS Nano* **10**, 2922–2929 (2016).

47. T. Ma, W. Ren, Z. Liu, L. Huang, L. P. Ma, X. Ma, Z. Zhang, L. M. Peng, H. M. Cheng, Repeated growth–etching–regrowth for large-area defect-free single-crystal graphene by chemical vapor deposition. *ACS Nano* **8**, 12806–12813 (2014).

48. N. Petrone, C. R. Dean, I. Meric, A. M. van der Zande, P. Y. Huang, L. Wang, D. Muller, K. L. Shepard, J. Hone, Chemical vapor deposition-derived graphene with electrical performance of exfoliated graphene. *Nano Lett.* **12**, 2751–2756 (2012).

49. A. C. Ferrari, J. C. Meyer, V. Scardaci, C. Casiraghi, M. Lazzeri, F. Mauri, S. Piscanec, D. Jiang, K. S. Novoselov, S. Roth, A. K. Geim, Raman spectrum of graphene and graphene layers. *Phys. Rev. Lett.* **97**, 187401 (2006).

50. V. I. Artyukhov, Y. Liu, B. I. Yakobson, Equilibrium at the edge and atomistic mechanisms of graphene growth. *Proc. Natl. Acad. Sci. U.S.A.* **109**, 15136–15140 (2012).

51. T. Wu, X. Zhang, Q. Yuan, J. Xue, G. Lu, Z. Liu, H. Wang, H. Wang, F. Ding, Q. Yu, X. Xie, M. Jiang, Fast growth of inch-sized single-crystalline graphene from a controlled single nucleus on Cu–Ni alloys. *Nat. Mater.* **15**, 43–47 (2016).

52. X. Li, C. W. Magnuson, A. Venugopal, R. M. Tromp, J. B. Hannon, E. M. Vogel, L. Colombo, R. S. Ruoff, Large-area graphene single crystals grown by low-pressure chemical vapor deposition of methane on copper. *J. Am. Chem. Soc.* **133**, 2816–2819 (2011).

53. K. Yan, D. Wu, H. Peng, L. Jin, Q. Fu, X. Bao, Z. Liu, Modulation-doped growth of mosaic graphene with single-crystalline p–n junctions for efficient photocurrent generation. *Nat. Commun.* **3**, 1280 (2012).

54. J. Li, L. Lin, D. Rui, Q. Li, J. Zhang, N. Kang, Y. Zhang, H. Peng, Z. Liu, H. Q. Xu, Electron–hole symmetry breaking in charge transport in nitrogen-doped graphene. *ACS Nano* **11**, 4641–4650 (2017).

55. Z. Jin, J. Yao, C. Kittrell, J. M. Tour, Large-scale growth and characterizations of nitrogen-doped monolayer graphene sheets. *ACS Nano* **5**, 4112–4117 (2011).

56. A. Zabet-Khosousi, L. Zhao, L. Pálová, M. S. Hybertsen, D. R. Reichman, A. N. Pasupathy, G. W. Flynn, Segregation of sublattice domains in nitrogen-doped graphene. *J. Am. Chem. Soc.* **136**, 1391–1397 (2014).

57. R. Lv, Q. Li, A. R. Botello-Méndez, T. Hayashi, B. Wang, A. Berkdemir, Q. Hao, A. L. Elías, R. Cruz-Silva, H. R. Gutiérrez, Y. A. Kim, H. Muramatsu, J. Zhu, M. Endo, H. Terrones, J. C. Charlier, M. Pan, M. Terrones, Nitrogen-doped graphene: Beyond single substitution and enhanced molecular sensing. *Sci. Rep.* **2**, 586 (2012).

58. K. Novoselov, A. K. Geim, S. V. Morozov, D. Jiang, M. I. Katsnelson, I. V. Grigorieva, S. V. Dubonos, A. A. Firsov, Two-dimensional gas of massless Dirac fermions in graphene. *Nature* **438**, 197–200 (2005).

59. F. Bonaccorso, Z. Sun, T. Hasan, A. Ferrari, Graphene photonics and optoelectronics. *Nat. Photonics* **4**, 611–622 (2010).

60. X. Li, Y. Zhu, W. Cai, M. Borysiak, B. Han, D. Chen, R. D. Piner, L. Colombo, R. S. Ruoff, Transfer of large-area graphene films for high-performance transparent conductive electrodes. *Nano Lett.* **9**, 4359–4363 (2009).

61. S. Tang, H. Wang, H. S. Wang, Q. Sun, X. Zhang, C. Cong, H. Xie, X. Liu, X. Zhou, F. Huang, X. Chen, T. Yu, F. Ding, X. Xie, M. Jiang, Silane-catalysed fast growth of large single-crystalline graphene on hexagonal boron nitride. *Nat. Commun.* **6**, 6499 (2015).

62. W. Yang, G. Chen, Z. Shi, C.-C. Liu, L. Zhang, G. Xie, M. Cheng, D. Wang, R. Yang, D. Shi, K. Watanabe, T. Taniguchi, Y. Yao, Y. Zhang, G. Zhang, Epitaxial growth of single-domain graphene on hexagonal boron nitride. *Nat. Mater.* **12**, 792–797 (2013).

Science Advances

Nitrogen cluster doping for high-mobility/conductivity graphene films with millimeter-sized domains

Li Lin, Jiayu Li, Qinghong Yuan, Qiucheng Li, Jincan Zhang, Luzhao Sun, Dingran Rui, Zhaolong Chen, Kaicheng Jia, Mingzhan Wang, Yanfeng Zhang, Mark H. Rummeli, Ning Kang, H. Q. Xu, Feng Ding, Hailin Peng and Zhongfan Liu

ARTICLE TOOLS	http://advances.sciencemag.org/content/5/8/eaaw8337
SUPPLEMENTARY MATERIALS	http://advances.sciencemag.org/content/suppl/2019/08/05/5.8.eaaw8337.DC1
REFERENCES	This article cites 62 articles, 7 of which you can access for free http://advances.sciencemag.org/content/5/8/eaaw8337#BIBL
PERMISSIONS	http://www.sciencemag.org/help/reprints-and-permissions

Use of this article is subject to the Terms of Service